

Spectrally Dispersed K -Band Interferometric Observations of Herbig Ae/Be Sources: Inner Disk Temperature Profiles

J.A. Eisner^{1,2}, E.I. Chiang^{1,3}, B.F. Lane^{4,5}, & R.L. Akeson⁶

jae@astro.berkeley.edu

ABSTRACT

We use spectrally dispersed near-IR interferometry data to constrain the temperature profiles of sub-AU-sized regions of 11 Herbig Ae/Be sources. We find that a single-temperature ring does not reproduce the data well. Rather, models incorporating radial temperature gradients are preferred. These gradients may arise in a dusty disk, or may reflect separate gas and dust components with different temperatures and spatial distributions. Comparison of our models with broadband spectral energy distributions suggests the latter explanation. The data support the view that the near-IR emission of Herbig Ae/Be sources arises from hot circumstellar dust and gas in sub-AU-sized disk regions. Intriguingly, our derived temperature gradients appear systematically steeper for disks around higher mass stars. It is not clear, however, whether this reflects trends in relative dust/gas contributions or gradients within individual components.

Subject headings: stars:pre-main sequence—stars:circumstellar matter—stars:individual(AB Aur, MWC 480, MWC 758, CQ Tau, T Ori, MWC 120, VV Ser, V1295 Aql, V1685 Cyg, AS 442, MWC 1080)—techniques:high angular resolution—techniques:interferometric

¹University of California at Berkeley, Department of Astronomy, 601 Campbell Hall, Berkeley, CA 94720

²Miller Fellow

³Alfred P. Sloan Research Fellow

⁴MIT Kavli Institute for Astrophysics and Space Research, MIT Department of Physics, 70 Vassar Street, Cambridge, MA 02139

⁵Pappalardo Fellow

⁶Michelson Science Center, California Institute of Technology, MC 100-22, Pasadena, CA 91125

1. INTRODUCTION

Disks of dust and gas around young stars provide laboratories for studying the initial conditions of planet formation. A knowledge of disk temperature profiles at stellocentric radii $R \lesssim 1$ AU is crucial for understanding both terrestrial and giant planet formation. Planet formation is only possible beyond the dust sublimation radius (where temperatures are $\lesssim 1500$ K), since dust is an essential building block of terrestrial planets and giant planet cores. The disk temperature profile also dictates the location of the “snowline” (e.g., Lecar et al. 2006), beyond which temperatures are low enough for water ice formation. The snowline tells us where icy material originates, which is important for understanding how water-rich, Earth-like planets come to be. Furthermore, because the surface density in solids is higher at and beyond the snowline, giant planet formation is facilitated there.

Spectral energy distributions (SEDs) provide some information about disk temperature profiles (e.g., Hillenbrand et al. 1992; Chiang & Goldreich 1997), but cannot provide unambiguous constraints. The addition of spatially resolved information breaks degeneracies inherent in SED modeling, and enables mapping of the density and temperature structure of disks (e.g., Eisner et al. 2005; van Boekel et al. 2004; Wilner et al. 2000). For example, near-IR interferometric observations have shown that simple geometrically thin disk models (e.g., Lynden-Bell & Pringle 1974; Adams, Lada, & Shu 1987) generally do not fit the data obtained for protoplanetary disks, while the inclusion of puffed-up inner disk edges (e.g., Dullemond et al. 2001) allows models to match the data well for most sources (e.g., Eisner et al. 2004, 2005).

To further constrain inner disk temperature profiles, spatially resolved observations at multiple wavelengths are necessary. Since dust (and gas) emission is temperature and wavelength dependent, different radial disk temperature profiles produce distinct spatial distributions of emission at different wavelengths. Thus, measurements of emission intensity and size as a function of wavelength can be used to determine inner disk temperature profiles.

Spectrally dispersed interferometry observations also have the potential to probe the spatial distribution of spectral line emission relative to continuum emission. Most of the mass in protoplanetary disks is contained in gas, which emits primarily through molecular and atomic transitions. Investigating spectral line emission is therefore crucial for understanding disk dynamics and the mass assembly and migration of gas giant planets.

Here we present observations that spatially resolve the K -band ($\lambda_0 = 2.2 \mu\text{m}$; $\Delta\lambda = 0.4 \mu\text{m}$) emission from protoplanetary disks around intermediate mass pre-main-sequence stars. These observations are also spectrally dispersed across 5 spectral channels ($R = 25$). We use these data to investigate the temperature profiles of disks at stellocentric radii less than 1

AU. We also explore whether disk models that include only emission from dust are sufficient to explain our observations or whether gaseous emission, including spectral line emission from hot water vapor or CO, needs to be considered.

2. OBSERVATIONS AND CALIBRATION

The Palomar Testbed Interferometer (PTI) is a long-baseline near-IR Michelson interferometer located on Palomar Mountain near San Diego, CA (Colavita et al. 1999). PTI combines starlight pairwise from three 40-cm aperture telescopes using a Michelson beam combiner, and the resulting fringe visibilities provide a measure of the brightness distribution on the sky (via the van Cittert-Zernike theorem). PTI measures normalized squared visibilities, V^2 , which provide unbiased estimates of the visibility amplitudes (Colavita 1999); V^2 is unity for point sources and smaller for resolved sources.

We observed 14 Herbig Ae/Be (HAEBE) sources with PTI between May 2002 and January 2004. Properties of the broadband K emission were reported previously in Eisner et al. (2003, 2004). Here we consider the subset of 11 objects that were spatially resolved (but not over-resolved) in the previous observations, and use the spectrally dispersed PTI data to examine trends in the visibilities with wavelength across a 5-channel “spectrum.” The K -band ($2.2 \mu\text{m}$) measurements were dispersed into 5 spatially filtered spectral channels on an 85-m North-West (NW) baseline for all 11 objects, on an 86-m South-West (SW) baseline for 8, and on a 110-m North-South (NS) baseline for 5. The NW baseline is oriented 109° west of north and has a fringe spacing of ~ 5 mas, the SW baseline is 211° west of north with a ~ 5 mas fringe spacing, and the NS baseline is 160° west of north and has a fringe spacing of ~ 4 mas.

Visibility data were measured in 130-second “scans,” which each consist of 5 equal time blocks. V^2 for the scan is given by the mean of these blocks, and the measurement uncertainty is the standard deviation. Measured V^2 for the science targets were calibrated by observing sources of known angular size and parallax (see Eisner et al. 2004 for details of calibrator sources). These calibrators were unresolved by the interferometer, and were close (within $\sim 10^\circ$) to the target sources on the sky; when calibrating a target source V^2 , data from different calibrators were weighted according to their proximity to the target in time and angle (e.g., Boden et al. 1998).

Based on previous observations of binary objects, the uncertainty in calibrated, broadband K -continuum V^2 measurements for PTI is $\sim 0.01 - 0.05$. The data in the narrow-band spectral channels typically have similar uncertainties. We verified this by calculating the

standard deviation of all V^2 measurements in each spectral channel (calibrated as described above) for an unresolved “check star” whose K magnitude is similar to those of our targets. The standard deviations of the V^2 values for the check star in spectral channels centered at 2.0, 2.1, 2.2, 2.3, and 2.4 μm are 0.05, 0.03, 0.02, 0.01, and 0.01, respectively. The larger values at the shortest wavelengths arise because absorption by atmospheric water vapor leads to lower fluxes. We adopt these values as the noise floors in each spectral channel for our science data.¹

We also discard a small amount of data for which low photon counts prevent the measurement of any meaningful signal. For very low photon counts the measured V^2 , which are unbiased, may be > 1 or < 0 because of large scatter (Colavita 1999). The discarded data are all from the shortest-wavelength channel, in which atmospheric water vapor absorption leads to lower photon counts. We eliminate all visibilities in the 2.0 μm channel from nights where the majority of the V^2 measurements in this channel are > 1 or < 0 .

We derive crude spectra from the observed count rates in our PTI data. We first normalize the photometry by dividing by the mean flux for all spectral channels, and then calibrate instrumental and atmospheric effects for this normalized photometry with the same stars used to calibrate the V^2 measurements. These main-sequence calibrator stars have spectral types ranging from F7 to A0, and nearly flat near-IR spectra ($H - K \lesssim 0.2$ based on 2MASS photometry). Since most calibrators are not colorless A0V stars, the calibrated fluxes for the target stars may have some residual slopes. However, this does not appear to be a significant effect. Figure 1 shows the fluxes for four of our target stars and one “check star,” all calibrated with the same set of calibrators. The check star exhibits a nearly flat spectrum, as expected based on the near-IR colors ($H - K \sim 0.1$ from 2MASS photometry). Thus, our differential spectral calibration appears reliable to within $\sim 10\%$. We estimate (conservatively) that relative (channel-to-channel) fluxes for our target objects have uncertainties of 20%. If we remove the continuum slopes of our targets, no significant flux variations are observed above the estimated 20% uncertainties.

One of our sample objects, MWC 1080, has a nearby companion with $0''.78$ separation and $\Delta K = 2.70$ (Eisner et al. 2004). Since we do not know the color of the companion star across the K band, we do not attempt to subtract contributions of the companion from our flux and V^2 data. Given the flux ratio of the two stars this may introduce additional uncertainties of $\sim 10\%$ in the modeling for this source. None of our other targets have known

¹The results discussed below do not change substantially if higher or lower noise floors are used. As expected, however, the uncertainties in fitted parameters are larger and the reduced χ^2 values of best-fit models are smaller if a higher noise floor is assumed (and vice versa for a lower noise floor).

companions which would influence the visibility data at the few percent level (Eisner et al. 2004).

3. MODELING AND RESULTS

Before modeling the circumstellar excess emission from our sample, we account for the effects of flux from the unresolved central star on the measured V^2 in §3.1. In §3.2, we fit a simple geometrical model to the V^2 data for each spectral channel individually; our intent is to provide a simple picture, with few assumptions, of how the emission size depends on wavelength. In §3.3, we then analyze as a whole our entire dataset of spectrally dispersed flux and V^2 measurements from 2.0–2.4 μm (§2), fitting disk models that account only for continuum emission to all of the data simultaneously. We consider a single-temperature ring model, a two-ring model, and a disk model for which the temperature decreases smoothly with radius. In §3.4 we investigate the possible effect of spectral line emission on the spectrally dispersed data. Finally we compute broadband spectral energy distributions (SEDs) for our best-fit models and compare these to observed SEDs from the literature in §3.5.

3.1. Circumstellar-to-Stellar Flux Ratios

In order to model the circumstellar emission, we must first estimate the contribution to the measured fluxes and V^2 from the unresolved central stars. Following previous investigators (e.g., Millan-Gabet et al. 2001), we use spectral decomposition to estimate the relative fluxes of the unresolved star and the circumstellar excess. We determine the stellar flux for our sample objects by fitting a blackbody to optical photometry (from the literature; see Eisner et al. 2004), and then extrapolating to the K -band. The excess flux is given by the difference between the observed flux and the estimated stellar flux. To convert the normalized 2.0–2.4 μm fluxes in each channel (§2) into absolute flux units, we use continuum K -band photometric flux measurements from Eisner et al. (2004). Derived circumstellar-to-stellar flux ratios for each spectral channel are listed in Table 1. Because the stellar flux declines precipitously with wavelength while the excess flux increases with wavelength, the circumstellar-to-stellar flux ratio increases steeply across the K -band.

As discussed in Eisner et al. (2004), uncertainties in the K -band photometric measurements and uncertainties in optical photometry lead to errors in the estimated circumstellar-to-stellar flux ratios of ~ 10 –20%. In addition, uncertainties in the channel-to-channel flux measurements (§2) introduce errors in the circumstellar-to-stellar flux ratios of ~ 10 –20%.

While many of our sample objects are variable at near-IR wavelengths (e.g., Skrutskie et al. 1996), the photometric K-band measurements were nearly contemporaneous with our PTI observations, and thus source variability should not be a major source of uncertainty. Thus the total uncertainties in estimated circumstellar-to-stellar flux ratios are $\sim 20\text{--}30\%$. These uncertainties lead to small errors in the fitted angular sizes because the near-IR emission from our sample is dominated by the circumstellar component; typical uncertainties on fitted parameters are a few percent (see Eisner et al. 2004).

3.2. Emission Radius versus Wavelength

Before considering the complete dataset, which consists of V^2 and fluxes measured in 5 spectral channels from 2.0 to 2.4 μm , we provide an estimate of angular size as measured in each spectral channel. We employ a simple model for the circumstellar excess emission, and fit this model to the V^2 measured in each spectral channel. Each source was observed multiple times over multiple baselines, and we fit all of the V^2 measurements in a given channel simultaneously.

Our chosen model is a uniform ring of fixed fractional width. The normalized V^2 of a ring, viewed face-on, is given by

$$V_{\text{ring}}^2 = \left(\frac{2\lambda}{\pi\theta_{\text{in}}r_{\text{uv}}(2f + f^2)} \left\{ (1 + f)J_1 \left(\frac{[1 + f]\pi\theta_{\text{in}}r_{\text{uv}}}{\lambda} \right) - J_1 \left(\frac{\pi\theta_{\text{in}}r_{\text{uv}}}{\lambda} \right) \right\} \right)^2, \quad (1)$$

where $\theta_{\text{in}}/2$ is the inner angular radius of the ring, $1 + f$ is the ratio of the outer ring radius to the inner ring radius, $r_{\text{uv}} = (u^2 + v^2)^{1/2}$ is the “uv radius,” u, v are the projected baseline lengths on the sky, and J_1 is a first-order Bessel function. We take $f = 0.2$ for all objects. The only free parameter in the model is θ_{in} .

Inclined geometries are included in this model, and in those discussed below, using a transformation to a circularly symmetric coordinate system (see e.g., Millan-Gabet et al. 2001; Eisner et al. 2003). We assume values for the inclination and position angle based on previous modeling of the broadband K emission (Eisner et al. 2004). We verified that these values were reasonable for the spectrally dispersed data by fitting ring models where inclination and position angle (in addition to θ_{in}) were free parameters. For all objects, the best-fit position angles and inclinations were consistent within the 1σ uncertainties across the 5 spectral channels. Furthermore, these values were compatible with those derived previously from wide-band V^2 measurements (Eisner et al. 2004). We therefore fix the inclinations and position angles in the modeling presented here.

Fitted inner ring radii as functions of wavelength are shown in Figure 2. We also indicate

the corresponding linear radii computed using the distances assumed in Eisner et al. (2004). Clearly, size increases with wavelength for most objects. Such behavior is expected for irradiated disks and/or accretion disks, where the temperature decreases with increasing stellocentric radius. It is not consistent with a single-temperature ring at fixed radius, since the angular size of such a ring is independent of wavelength. For several objects, the inferred sizes are not obviously increasing with wavelength. Rather, the size of the circumstellar emission is independent of λ within uncertainties (e.g., V1295 Aql), or is not a monotonic function (e.g., V1685 Cyg).

3.3. Circumstellar Emission Models

To quantitatively investigate the radial temperature structure suggested by Figure 2, in this section we fit simple models to our V^2 and photometry data for all spectral channels simultaneously. Here we assume that the models emit only continuum emission; in §3.4 we investigate whether better fits are obtained when spectral line emission is included. For all models we fit only our V^2 and flux data measured from 2.0–2.4 μm ; in §3.5 we compute the broadband SEDs predicted by our best-fit models and compare to observations.

3.3.1. Single-Temperature Ring

We first consider the uniform ring model discussed above, but now fit the model to the complete dataset all at once (instead of fitting each channel individually). In addition, we now consider the measured fluxes as well as V^2 . This necessitates the introduction of a ring temperature, T_{ring} , in order to fit the photometry data. If we assume for simplicity that the ring emits as a blackbody, the flux emitted by the ring is

$$F_\nu(R) = \frac{2\pi \cos i}{d^2} B_\nu(T_{\text{ring}}) R_{\text{in}}^2 (f + f^2/2) \approx \frac{2\pi \cos i}{d^2} B_\nu(T_{\text{ring}}) R_{\text{in}}^2 f. \quad (2)$$

Here B_ν is the Planck function, d is the distance, and i is the inclination of the ring (d and i are assigned from Eisner et al. 2004). We determine the values of R_{in} and T_{ring} that provide the best fit to all of the measured V^2 and fluxes for a given source (Table 2).

It is not surprising that the reduced χ^2 values of our best-fit ring models are > 1 (Table 2), since the ring model produces the same size in each channel, contrary to what is observed in the data (see §3.2). We illustrate the poorness of fit with an example in Figure 3, which shows the measured V^2 along with the prediction of the best-fit single-temperature ring model for AB Aur. While χ_r^2 is not far from unity for several objects, this is probably because

of large measurement errors and does not necessarily imply that the single-temperature ring model provides a good physical description of the data.

3.3.2. Two Rings

The dependence of source angular size on wavelength suggests that we should include temperature-dependent radial gradients in the models. While a single-temperature ring model possesses no such gradients, the addition of a second ring at different stellocentric radius and temperature will lead to observed source structure that is a function of wavelength. Specifically, the cooler, outer ring will contribute relatively more emission at longer wavelengths, and thus the angular size of the two-ring model will tend to increase with wavelength.

We assume the rings have fractional widths of 0.2, and we fix the radius of the inner ring at 0.1 AU. So long as the inner ring is essentially unresolved by our observations, the exact choice of inner ring radius will not substantially alter the quality of the fits. We verified this by performing fits where the inner ring radius was left as a free parameter; reduced χ^2 values did not improve with this extra degree of freedom. Smaller assumed values of the inner ring radius will, however, yield higher inner ring temperatures. Conversely, larger values of the inner ring radius give lower inner ring temperatures. However substantially larger inner ring radii can be ruled out since they would be spatially resolved, and would thus lower the quality of the fits.

The free parameters of the model are the temperature of the inner ring, and the radius and temperature of the outer ring. This is obviously a simple description of a potentially complex system, but will demonstrate whether a multi-component continuum model is suitable for explaining our data. As above, the data fitted include V^2 and fluxes measured from 2.0–2.4 μm (§2).

V^2 values predicted by best-fit two-ring models are shown in Figure 4. Best-fit parameters and reduced χ^2 values are listed in Table 3. For objects that display a monotonic increase in size with wavelength (see Figure 2) the reduced χ^2 values for this model are lower than for the single ring model (§3.3.1). In contrast, for T Ori, V1295 Aql, V1685 Cyg, and AS 442, sources for which the size does not appear to increase with wavelength, the single-temperature ring model provides a lower reduced χ^2 . The high temperature of the inner ring for MWC 1080 is due to our assumed inner ring radius of 0.1 AU. A larger inner ring radius—which would lead to a lower fitted inner ring temperature—is compatible with our data; at the source distance (~ 1 kpc; see Eisner et al. 2003), an inner ring radius as

large as ~ 0.5 AU would still produce unresolved emission as assumed in our model.

3.3.3. Disk with Smooth Radial Temperature Gradient

As a generalization of the two-ring model (§3.3.2), we construct a disk model with a continuous temperature gradient. If the temperature decreases over a range of disk radii then the cooler material at larger radii may contribute relatively more emission at longer wavelengths. We consider a disk model with a power-law temperature profile,

$$T = T_{\text{in}} \left(\frac{R}{R_{\text{in}}} \right)^{-\alpha}. \quad (3)$$

Here, R is the stellocentric radius, R_{in} is the inner radius of the disk, and T_{in} is the temperature at $R = R_{\text{in}}$. The model is described by three free parameters: R_{in} , T_{in} , and α .

We assume the model extends from R_{in} to an outer radius $R_{\text{out}} = 10$ AU. The exact choice of R_{out} is not crucial since most of the $2 \mu\text{m}$ emission arises from sub-AU radii. However if R_{out} is $\ll 1$ AU then the model will not produce substantially different angular sizes at different radii; rather the emission would appear to arise from a narrow ring at all wavelengths and the model would resemble the single-temperature ring model described in §3.3.1. To explain the dependence of angular size on wavelength, we require $R_{\text{out}} \gtrsim 1$ AU.

We divide the disk up into annuli and compute the flux and visibilities for each annulus. We assume each annulus emits as a blackbody so that the flux in an annulus of infinitesimal width dR (observed at the Earth) is

$$dF_{\nu}(R) = \frac{2\pi \cos i}{d^2} B_{\nu}(T) R dR, \quad (4)$$

where B_{ν} is the Planck function, d is the distance, and i is the disk inclination. The normalized visibilities for an annulus extending from R_1 to $R_2 = R_1 + dR$ are given by the difference of visibilities for uniform disks having radii equal to R_1 and R_2 :

$$V(R) = \frac{\lambda d}{\pi r_{\text{uv}}(R_2^2 - R_1^2)} \left[R_2 J_1 \left(\frac{2\pi r_{\text{uv}} R_2}{\lambda d} \right) - R_1 J_1 \left(\frac{2\pi r_{\text{uv}} R_1}{\lambda d} \right) \right]. \quad (5)$$

The sum of dF_{ν} over all annuli gives the total disk flux, F_{ν} . The square of the flux-weighted sum of $V(R)$ over all annuli gives V^2 .

The V^2 values predicted by best-fit models including a temperature gradient in the inner disk are shown in Figure 4. Table 4 shows that the reduced χ^2 values of the best fits are generally $\lesssim 1$. For all objects except V1295 Aql and V1685 Cyg this model provides a

better fit (i.e., a lower reduced χ^2 value) than the single-temperature ring model. Moreover, the temperature gradient model yields a better fit to the data than the two-ring model for all sources. Thus, our spectrally dispersed interferometry data favor disk models that incorporate radial temperature gradients. How well the temperature gradient model fits broadband SEDs compared to other models is discussed in §3.5.

For most sources the inner disk sizes and temperatures derived here are similar to those inferred by Eisner et al. (2004) from broadband (2.0–2.4 μm) V^2 measurements. This is expected since the broadband V^2 measurements from Eisner et al. (2004) have similar values to the spectrally dispersed measurements presented here. However, for objects with small best-fit α values (e.g., MWC 758 or CQ Tau), our determined inner radii are smaller than the previous estimates by $\lesssim 40\%$. This discrepancy is due to the fact that Eisner et al. (2004) assumed $\alpha = 0.75$ for their disk models; for the smaller α values inferred here, the inner edge of the disk must extend further inward to match the data. The values of R_{in} determined here are more reliable than previous estimates since α and R_{in} have been determined simultaneously.

3.4. Spectral Line Emission

While disk models including only continuum emission can provide reasonable fits to our spectrally dispersed interferometry data, several objects—T Ori, V1295 Aql, V1685 Cyg, and AS 442—do not show the monotonic increase of size with wavelength expected for the continuum models with temperature gradients (§§3.3.2–3.3.3). This is particularly striking for V1685 Cyg, where the smaller uncertainties strongly imply non-monotonic dependence of size on wavelength (see Figure 2). One potential explanation is that gaseous emission, with a different spatial scale than the dust continuum, contributes to the visibilities in certain spectral channels.

Based on compilations of H₂O and CO emission lines from the HITRAN database (Rothman et al. 2005), gaseous spectral line emission, if present, contributes principally to the PTI measurements in the channels centered at 2.0, 2.3, and 2.4 μm (Figure 5). Previous observations of hot gas near a young star illustrate that gaseous emission features may be quite broad (Carr et al. 2004), and thus this emission might fill large parts of some spectral channels.

If the dust and gas emission components have different spatial distributions, then the visibilities in spectral channels where gaseous emission is important (2.0, 2.3, and 2.4 μm) may be offset from the visibilities in spectral channels dominated by dust continuum emission

(2.1 and 2.2 μm). This effect has been observed previously in evolved late-type stars, where molecular layers above the stellar photosphere lead to different measured sizes across the K -band (e.g., Thompson et al. 2002). To investigate whether gaseous emission is contributing to our measured visibilities, we fit the models discussed above to only the visibilities measured from 2.1 to 2.2 μm , and compare these fits to those using the data from all channels.

Best-fit parameters for “continuum”-only fits (i.e., fits using only the data measured from 2.1 to 2.2 μm) are included in Table 4, and the predicted V^2 values are plotted in Figure 4. For all sources, the best-fit inner disk sizes for “continuum” channels only and for all channels are equal within the 1σ uncertainties. While the reduced χ^2 values of the “continuum”-only fits are smaller for AB Aur, T Ori, VV Ser, AS 442, and MWC 1080 (Table 4), the differences are small for all sources except AB Aur.

The incompatibility of a simple disk model with the observed size versus wavelength for V1685 Cyg was our main impetus for investigating gaseous emission. However, even if we consider only channels that are not expected to be contaminated by gaseous emission, the data are still not fitted well by our disk models (note the large χ_r^2 values in Table 4); the circumstellar emission for this object may not be represented well by a pure disk model.

The spectrally dispersed interferometry data presented here do not argue strongly for the presence of gaseous spectral line emission in the inner disks around our sample HAEBE stars. We also do not observe any strong gaseous emission features in our crude spectra (e.g., Figure 1). However the large uncertainties do not rule out gaseous spectral line emission with line-to-continuum ratios $\lesssim 20\%$. Furthermore, the smaller χ_r^2 values of continuum-only fits for several objects (especially AB Aur) are intriguing.

3.5. Spectral Energy Distributions

We fitted the models described above to measured V^2 and fluxes measured from 2.0–2.4 μm . We now compare the broadband fluxes predicted by our best-fit models to observed SEDs. This comparison is motivated by previous analyses of SEDs and K -band interferometry (e.g., Millan-Gabet et al. 2001; Eisner et al. 2004), which showed that single-temperature ring models generally provided better fits to the data than disks with temperature gradients.

Figure 7 shows the predicted and observed SEDs for our sample. Disk models incorporating smooth temperature gradients do not fit the SED data as well as the two other models for almost all objects; the SEDs are fitted better by single-temperature ring models or by two-ring models. One exception is MWC 1080, for which a disk model fits the SED data well; for this source the two-ring model does not fit the SED well (Figure 7). This is

consistent with previous arguments that early-type stars like MWC 1080 are surrounded by geometrically thin disks with temperature gradients (e.g., Eisner et al. 2004).

4. DISCUSSION

The size of the near-IR emission for most of our objects varies as a function of wavelength, indicating that a simple, single-temperature ring model for the emission is untenable; such a model predicts the same size regardless of observing wavelength. We showed above that the V^2 and flux data measured from 2.0–2.4 μm are fitted better by models incorporating radial temperature gradients.

Early puffed-up inner disk models (e.g., Dullemond et al. 2001) generally assumed that the inner wall emits as a single-temperature blackbody; this model resembled a single-temperature ring. Even if temperature gradients within the puffed-up inner rim are included (e.g., Isella & Natta 2005), the narrow range of radii over which the emission arises means that these models still resemble single-temperature rings. Our data therefore suggest that puffed-up inner rims alone do not fully represent the circumstellar emission from HAEBE sources.

Temperature gradients over a range of disk radii must be included in the model to fit the observational data presented here. The best fits to our spectrally-dispersed interferometry are obtained for two-ring models or models with power-law disk temperature profiles. Comparison of our models with broadband SEDs suggests that two-ring models are preferable. We suggest that our two-ring model represents a puffed-up edge of the dust disk and hotter inner disk gas. The best-fit temperatures of the inner ring are substantially hotter than the dust sublimation temperature, supporting our hypothesis that such emission probably traces gas. The outer rings have temperatures less than or comparable to the dust sublimation temperature, suggesting that the outer ring emission can arise from dust.

If inner disk/ring temperatures larger than dust sublimation temperatures reflect contributions from hot gas emission to measured fluxes and V^2 , we might also expect to detect variations in the visibilities as a function of wavelength due to gaseous CO or H₂O emission features. In general, no such trends are seen in our data (§3.4). It is possible that the gaseous emission features are so broad that they produce a “pseudo-continuum”; there is some support for this suggestion from previous observations of broad gaseous emission features from a young star (Carr et al. 2004). It is interesting to note, however, that for AB Aur, AS 442, and MWC 1080, objects with higher inner disk temperatures, there is a suggestion that the inclusion of gaseous emission features in the models would improve the fits to the observa-

tions, since the “continuum”-only models yield lower reduced χ^2 values than the fits where all the data is used (§3.4). Future observations with better spectral resolution are needed to probe potential spectral line emission in more detail.

While a two-ring model provides the best match to the combination of spectrally dispersed and SED data, a disk model with a radial temperature gradient provides the best fit to the spectrally dispersed interferometry data (from 2.0–2.4 μm) for all sources. Our results suggest that a multi-component model that includes temperature gradients in one or more components may provide better fits to the data than the simple models considered here. We note that MWC 1080, the most massive star in our sample, provides an exception: disk models with smooth temperature gradients fit all of the data well.

We discern a striking correlation between temperature gradient and effective temperature of the host star T_* , which may reflect relative differences in the dust/gas components or variations in the gradients within individual components. Using our power-law disk model, $T = T_{\text{in}}(R/R_{\text{in}})^{-\alpha}$, to illustrate this trend, we plot α as a function of T_* in Figure 6. Larger values of α (steeper gradients) are associated with objects with earlier spectral types. For MWC 480, MWC 758, CQ Tau, and T Ori, the objects in our sample with the latest spectral types, the best-fit models require $\alpha = 0.40$ – 0.55 . In contrast, inferred values of α for other objects in our sample range between 0.60 and 1.0.

There is some degeneracy between temperature profiles and optical depth profiles. In our modeling we assumed the emission was optically thick. The fitted inner disk and ring temperatures may be underestimated to the extent that the optical depth of the emitting region, τ_ν , is < 1 . By the same token, radial gradients in τ_ν are somewhat degenerate with temperature gradients. However, since τ_ν is likely to decrease with increasing radius and wavelength (e.g., $\tau_\nu \propto R^{-1}$ for the surface layers of geometrically thin disks; Chiang & Goldreich 1997), τ_ν gradients are more likely to produce larger sizes at shorter wavelengths (since more material at larger radii becomes optically thick). The gradients inferred from our data are therefore likely tracing temperature profiles as opposed to optical depth profiles.

5. CONCLUSIONS

We presented near-IR interferometry data, spectrally dispersed across 5 channels from 2.0 to 2.4 μm , from the Palomar Testbed Interferometer. These data were used to constrain the temperature profiles of sub-AU-sized regions of 11 Herbig Ae/Be disks. We found that a single-temperature ring of emission did not fit the spectrally dispersed data well. Two rings at different stellocentric radii and with different temperatures provide better fits to the data.

The best fits (i.e., yielding the lowest reduced χ^2 values) are for disk models incorporating smooth radial temperature gradients.

However, the smooth gradient disk models do not match broadband SEDs nearly as well as two-ring models. We therefore speculate that multiple emission components, probably dust and gas, at different temperatures and stellocentric radii are contributing to the observed data. More complex two-component models, including temperature gradients in one or both components, will better match the observations.

The inferred temperature profiles are systematically shallower for disks around less massive stars. However, it is unclear whether this indicates relative differences in the properties of the two components (gas and dust) as a function of spectral type, or whether this trend traces temperature gradients within a single component.

We also investigated whether gaseous emission, potentially at different spatial scales than the dust emission, contributes spectral line flux to our measurements. Because CO and H₂O are expected to emit primarily in the edge channels of our spectrally dispersed measurements, we performed fits of our disk models to only the central channels. Some objects showed a slight reduction (and in the case of AB Aur, a substantial reduction) in the reduced χ^2 values of the best-fit models when only the central channels were used. However, the best-fit parameters for fits to the central channels and those for fits to all data are consistent within the 1σ uncertainties for all objects. We are therefore unable to claim strong evidence for spectral line emission in the inner disks of our sample based on our current data. Given the evidence for hot inner disk continuum emission, future observations with better spectral resolution and sensitivity are warranted to further investigate inner disk gas in these objects.

Acknowledgments. The near-IR interferometry data presented in this paper were obtained at the Palomar Observatory using the Palomar Testbed Interferometer, which is supported by NASA contracts to the Jet Propulsion Laboratory. Science operations with PTI are possible through the efforts of the PTI Collaboration (<http://pti.jpl.nasa.gov/ptimembers.html>) and Kevin Rykoski. This research made use of software from the Michelson Science Center at the California Institute of Technology, and data products from 2MASS. J.A.E. is supported by a Miller Research Fellowship, E.I.C. acknowledges support from an Alfred P. Sloan Fellowship, and B.F.L. acknowledges support from a Pappalardo Fellowship in Physics.

REFERENCES

Adams, F. C., Lada, C. J., & Shu, F. H. 1987, ApJ, 312, 788

- Boden, A. F., Colavita, M. M., van Belle, G. T., & Shao, M. 1998, in *Proc. SPIE Vol. 3350*, 872–880, *Astronomical Interferometry*, Robert D. Reasenberg, Ed.
- Carr, J. S., Tokunaga, A. T., & Najita, J. 2004, *ApJ*, 603, 213
- Chiang, E. I. & Goldreich, P. 1997, *ApJ*, 490, 368
- Colavita, M. M. 1999, *PASP*, 111, 111
- Colavita, M. M., Wallace, J. K., Hines, B. E., Gursel, Y., Malbet, F., Palmer, D. L., Pan, X. P., Shao, M., Yu, J. W., Boden, A. F., Dumont, P. J., Gubler, J., Koresko, C. D., Kulkarni, S. R., Lane, B. F., Mobley, D. W., & van Belle, G. T. 1999, *ApJ*, 510, 505
- Dullemond, C. P., Dominik, C., & Natta, A. 2001, *ApJ*, 560, 957
- Eisner, J. A., Hillenbrand, L. A., White, R. J., Akeson, R. L., & Sargent, A. I. 2005, *ApJ*, 623, 952
- Eisner, J. A., Lane, B. F., Akeson, R. L., Hillenbrand, L., & Sargent, A. 2003, *ApJ*, 588, 360
- Eisner, J. A., Lane, B. F., Hillenbrand, L., Akeson, R., & Sargent, A. 2004, *ApJ*, 613, 1049
- Hillenbrand, L. A., Strom, S. E., Vrba, F. J., & Keene, J. 1992, *ApJ*, 397, 613
- Isella, A. & Natta, A. 2005, *A&A*, 438, 899
- Lecar, M., Podolak, M., Sasselov, D., & Chiang, E. 2006, *ApJ*, 640, 1115
- Lynden-Bell, D. & Pringle, J. E. 1974, *MNRAS*, 168, 603
- Millan-Gabet, R., Schloerb, F. P., & Traub, W. A. 2001, *ApJ*, 546, 358
- Monnier, J. D. & Millan-Gabet, R. 2002, *ApJ*, 579, 694
- Monnier, J. D., Millan-Gabet, R., Billmeier, R., Akeson, R. L., Wallace, D., Berger, J.-P., Calvet, N., D’Alessio, P., Danchi, W. C., Hartmann, L., Hillenbrand, L. A., Kuchner, M., Rajagopal, J., Traub, W. A., Tuthill, P. G., Boden, A., Booth, A., Colavita, M., Gathright, J., Hrynevych, M., Le Mignant, D., Ligon, R., Neyman, C., Swain, M., Thompson, R., Vasisht, G., Wizinowich, P., Beichman, C., Beletic, J., Creech-Eakman, M., Koresko, C., Sargent, A., Shao, M., & van Belle, G. 2005, *ApJ*, 624, 832
- Pollack, J. B., Hollenbach, D., Beckwith, S., Simonelli, D. P., Roush, T., & Fong, W. 1994, *ApJ*, 421, 615

- Rothman, L. S., Jacquemart, D., Barbe, A., Benner, D. C., Birk, M., Brown, L. R., Carleer, M. R., Chackerian, C., Chance, K., Coudert, L. H., Dana, V., Devi, V. M., Flaud, J. M., Gamache, R. R., Goldman, A., Hartmann, J. M., Jucks, K. W., Maki, A. G., Mandin, J. Y., Massie, S. T., Orphal, J., Perrin, A., Rinsland, C. P., Smith, M. A. H., Tennyson, J., Tolchenov, R. N., Toth, R. A., Vander Auwera, J., Varanasi, P., & Wagner, G. 2005, *Journal of Quantitative Spectroscopy and Radiative Transfer*, 96, 139
- Skrutskie, M.F., Meyer, M.R., Whalen, D., & Hamilton, C. 1996, *AJ*, 112, 2168
- Thompson, R. R., Creech-Eakman, M. J., & van Belle, G. T. 2002, *ApJ*, 577, 447
- van Boekel, R., Min, M., Leinert, C., Waters, L. B. F. M., Richichi, A., Chesneau, O., Dominik, C., Jaffe, W., Dutrey, A., Graser, U., Henning, T., de Jong, J., Köhler, R., de Koter, A., Lopez, B., Malbet, F., Morel, S., Paresce, F., Perrin, G., Preibisch, T., Przygodda, F., Schöller, M., & Wittkowski, M. 2004, *Nature*, 432, 479
- Wilner, D. J., Ho, P. T. P., Kastner, J. H., & Rodríguez, L. F. 2000, *ApJ*, 534, L101

Table 1. Circumstellar-to-Stellar Flux Ratios from 2.0 – 2.4 μm

Source	$r_{2.0 \mu\text{m}}$	$r_{2.1 \mu\text{m}}$	$r_{2.2 \mu\text{m}}$	$r_{2.3 \mu\text{m}}$	$r_{2.4 \mu\text{m}}$
AB Aur	3.8	4.7	5.8	7.0	8.2
MWC 480	2.0	2.6	3.2	3.9	4.6
MWC 758	3.3	4.1	5.0	6.0	7.0
CQ Tau	2.5	3.3	4.2	5.1	6.1
T Ori	5.3	6.7	8.5	10.3	12.0
MWC 120	4.9	6.3	7.8	9.5	11.2
VV Ser	6.5	8.2	10.6	13.1	15.6
V1295 Aql	1.5	2.0	2.6	3.3	4.0
V1685 Cyg	3.7	4.7	6.2	7.6	9.1
AS 442	3.6	4.7	6.2	7.7	9.1
MWC 1080	5.2	7.0	9.1	11.6	14.1

Note. — r_λ denotes the ratio of the circumstellar excess emission to the stellar photospheric emission. This ratio is calculated for each of the PTI spectral channels, and typical uncertainties are $\sim 20\text{--}30\%$ (§3.1).

Table 2. Best fits for single-temperature ring models

Source	χ_r^2	$\theta_{\text{in}}/2$ (mas)	R_{in} (AU)	T_{ring} (K)
AB Aur	2.346	$1.64_{-0.01}^{+0.01}$	$0.23_{-0.01}^{+0.01}$	$1860.0_{-60.0}^{+60.0}$
MWC 480	1.153	$1.51_{-0.01}^{+0.01}$	$0.21_{-0.01}^{+0.01}$	$1440.0_{-40.0}^{+40.0}$
MWC 758	2.267	$1.30_{-0.01}^{+0.01}$	$0.20_{-0.01}^{+0.01}$	$1600.0_{-50.0}^{+40.0}$
CQ Tau	1.179	$1.36_{-0.01}^{+0.02}$	$0.20_{-0.01}^{+0.01}$	$1420.0_{-40.0}^{+30.0}$
T Ori	0.904	$0.87_{-0.03}^{+0.02}$	$0.39_{-0.01}^{+0.01}$	$1640.0_{-60.0}^{+50.0}$
MWC 120	1.173	$1.52_{-0.01}^{+0.01}$	$0.76_{-0.01}^{+0.01}$	$1560.0_{-50.0}^{+40.0}$
VV Ser	1.164	$1.44_{-0.03}^{+0.02}$	$0.45_{-0.01}^{+0.01}$	$1500.0_{-50.0}^{+40.0}$
V1295 Aql	1.005	$1.70_{-0.01}^{+0.01}$	$0.49_{-0.01}^{+0.01}$	$1320.0_{-40.0}^{+20.0}$
V1685 Cyg	4.101	$1.16_{-0.01}^{+0.01}$	$1.16_{-0.01}^{+0.01}$	$1760.0_{-60.0}^{+50.0}$
AS 442	1.125	$0.87_{-0.04}^{+0.03}$	$0.52_{-0.02}^{+0.02}$	$1840.0_{-80.0}^{+80.0}$
MWC 1080	1.840	$1.34_{-0.01}^{+0.01}$	$1.34_{-0.01}^{+0.01}$	$2300.0_{-110.0}^{+90.0}$

Note. — Linear inner ring radii, R_{in} , are computed using the derived angular inner radii, $\theta_{\text{in}}/2$, and the distances employed by Eisner et al. (2004).

Table 3. Best fits for two-ring models

Source	χ_r^2	$T_{\text{ring},1}$ (K)	$\theta_{\text{in},2}/2$ (mas)	$R_{\text{in},2}$ (AU)	$T_{\text{ring},2}$ (K)
AB Aur	1.769	$2310.0^{+140.0}_{-150.0}$	$2.14^{+0.09}_{-0.09}$	$0.30^{+0.01}_{-0.01}$	$1460.0^{+60.0}_{-70.0}$
MWC 480	0.841	$1710.0^{+80.0}_{-90.0}$	$2.13^{+0.11}_{-0.16}$	$0.30^{+0.02}_{-0.02}$	$1130.0^{+60.0}_{-50.0}$
MWC 758	1.256	$2010.0^{+90.0}_{-90.0}$	$2.24^{+0.01}_{-0.13}$	$0.34^{+0.01}_{-0.02}$	$1060.0^{+40.0}_{-20.0}$
CQ Tau	1.107	$1760.0^{+80.0}_{-140.0}$	$2.20^{+0.04}_{-0.41}$	$0.33^{+0.01}_{-0.06}$	$1010.0^{+130.0}_{-10.0}$
T Ori	1.139	$3100.0^{+690.0}_{-920.0}$	$1.24^{+0.53}_{-0.24}$	$0.56^{+0.24}_{-0.11}$	$1220.0^{+270.0}_{-220.0}$
MWC 120	0.868	$3850.0^{+140.0}_{-880.0}$	$1.83^{+0.11}_{-0.16}$	$0.92^{+0.06}_{-0.08}$	$1350.0^{+100.0}_{-80.0}$
VV Ser	1.111	$2740.0^{+310.0}_{-460.0}$	$1.91^{+0.23}_{-0.24}$	$0.59^{+0.07}_{-0.07}$	$1200.0^{+130.0}_{-90.0}$
V1295 Aql	1.174	$1500.0^{+320.0}_{-10.0}$	$1.78^{+0.12}_{-0.02}$	$0.52^{+0.03}_{-0.01}$	$1270.0^{+40.0}_{-60.0}$
V1685 Cyg	4.195	$1710.0^{+2280.0}_{-210.0}$	$1.16^{+0.05}_{-0.01}$	$1.17^{+0.05}_{-0.01}$	$1750.0^{+80.0}_{-90.0}$
AS 442	1.187	$3580.0^{+410.0}_{-640.0}$	$1.00^{+0.12}_{-0.01}$	$0.60^{+0.07}_{-0.01}$	$1590.0^{+70.0}_{-180.0}$
MWC 1080	1.224	$27060.0^{+5540.0}_{-8000.0}$	$1.73^{+0.07}_{-0.12}$	$1.73^{+0.07}_{-0.13}$	$1740.0^{+90.0}_{-250.0}$

Note. — Values of $R_{\text{in},2}$, are computed using the derived angular inner radii, $\theta_{\text{in},2}/2$, and the distances employed by Eisner et al. (2004). We have assumed an inner ring radius $R_{\text{in},1}=0.1$ AU for these models; the high inner ring temperature for MWC 1080 may indicate that a larger value of $R_{\text{in},1}$ is warranted for this source (§3.3.2).

Table 4. Best fits for disk models with temperature gradients

Source	T_* (K)	χ_r^2	$\theta_{\text{in}}/2$ (mas)	R_{in} (AU)	α	T_{in} (K)
Best-Fit Disk Models						
CQ Tau	7580	0.976	$0.60^{+0.29}_{-0.18}$	$0.09^{+0.04}_{-0.03}$	$0.40^{+0.15}_{-0.05}$	$1360.0^{+80.0}_{-60.0}$
MWC 758	8720	1.117	$0.63^{+0.02}_{-0.12}$	$0.09^{+0.01}_{-0.02}$	$0.45^{+0.05}_{-0.05}$	$1490.0^{+50.0}_{-50.0}$
T Ori	8720	0.759	$0.42^{+0.34}_{-0.32}$	$0.19^{+0.15}_{-0.14}$	$0.50^{+0.50}_{-0.15}$	$1580.0^{+550.0}_{-80.0}$
MWC 480	8970	0.780	$1.03^{+0.11}_{-0.15}$	$0.14^{+0.01}_{-0.02}$	$0.55^{+0.10}_{-0.10}$	$1340.0^{+40.0}_{-50.0}$
AB Aur	9520	1.657	$1.17^{+0.09}_{-0.06}$	$0.16^{+0.01}_{-0.01}$	$0.70^{+0.10}_{-0.05}$	$1700.0^{+80.0}_{-70.0}$
VV Ser	9520	1.029	$1.00^{+0.24}_{-0.22}$	$0.31^{+0.07}_{-0.07}$	$0.65^{+0.35}_{-0.15}$	$1430.0^{+80.0}_{-50.0}$
MWC 120	10500	0.524	$1.06^{+0.26}_{-0.22}$	$0.53^{+0.13}_{-0.11}$	$0.60^{+0.40}_{-0.15}$	$1440.0^{+120.0}_{-70.0}$
V1295 Aql	10500	1.068	$1.51^{+0.02}_{-0.12}$	$0.44^{+0.01}_{-0.04}$	$1.00^{+0.05}_{-0.25}$	$1330.0^{+30.0}_{-70.0}$
AS 442	11900	1.107	$0.49^{+0.26}_{-0.38}$	$0.29^{+0.16}_{-0.23}$	$0.60^{+0.40}_{-0.20}$	$1750.0^{+730.0}_{-90.0}$
V1685 Cyg	22000	4.158	$0.96^{+0.01}_{-0.04}$	$0.97^{+0.01}_{-0.05}$	$1.00^{+0.05}_{-0.10}$	$1710.0^{+70.0}_{-60.0}$
MWC 1080	30000	1.119	$0.79^{+0.10}_{-0.08}$	$0.79^{+0.11}_{-0.08}$	$0.65^{+0.10}_{-0.05}$	$2060.0^{+90.0}_{-100.0}$
“Continuum”-Only Fits						
CQ Tau	7580	1.078	$1.16^{+0.04}_{-0.46}$	$0.17^{+0.01}_{-0.07}$	$1.00^{+0.05}_{-0.55}$	$1440.0^{+60.0}_{-140.0}$
MWC 758	8720	1.218	$0.71^{+0.18}_{-0.19}$	$0.11^{+0.03}_{-0.03}$	$0.50^{+0.15}_{-0.10}$	$1500.0^{+70.0}_{-90.0}$
T Ori	8720	0.648	$0.23^{+0.51}_{-0.13}$	$0.11^{+0.23}_{-0.06}$	$0.40^{+0.60}_{-0.05}$	$1740.0^{+410.0}_{-270.0}$
MWC 480	8970	0.972	$0.96^{+0.24}_{-0.19}$	$0.14^{+0.03}_{-0.03}$	$0.50^{+0.25}_{-0.10}$	$1330.0^{+80.0}_{-70.0}$
AB Aur	9520	0.712	$1.16^{+0.19}_{-0.23}$	$0.16^{+0.03}_{-0.03}$	$0.70^{+0.30}_{-0.20}$	$1700.0^{+190.0}_{-140.0}$
VV Ser	9520	0.709	$1.03^{+0.21}_{-0.27}$	$0.32^{+0.06}_{-0.09}$	$0.70^{+0.30}_{-0.20}$	$1450.0^{+130.0}_{-100.0}$
MWC 120	10500	0.737	$1.26^{+0.04}_{-0.54}$	$0.63^{+0.02}_{-0.27}$	$1.00^{+0.05}_{-0.60}$	$1570.0^{+70.0}_{-210.0}$
V1295 Aql	10500	1.126	$1.54^{+0.03}_{-0.33}$	$0.45^{+0.01}_{-0.10}$	$1.00^{+0.05}_{-0.50}$	$1320.0^{+60.0}_{-130.0}$
AS 442	11900	0.978	$0.10^{+0.34}_{-0.00}$	$0.06^{+0.20}_{-0.00}$	$0.35^{+0.15}_{-0.05}$	$2260.0^{+80.0}_{-590.0}$
V1685 Cyg	22000	5.582	$1.00^{+0.01}_{-0.20}$	$1.00^{+0.02}_{-0.21}$	$1.00^{+0.05}_{-0.35}$	$1690.0^{+100.0}_{-120.0}$
MWC 1080	30000	1.008	$0.83^{+0.20}_{-0.20}$	$0.84^{+0.21}_{-0.20}$	$0.70^{+0.30}_{-0.15}$	$2060.0^{+220.0}_{-150.0}$

Note. — The stellar effective temperatures, T_* , are based on the assigned spectral types from Eisner et al. (2004). Linear inner radii, R_{in} , are computed using the derived angular inner radii, $\theta_{\text{in}}/2$, and the distances employed by Eisner et al. (2004). Objects are listed in order of increasing T_* to illustrate the correlation of T_* with R_{in} , α , and T_{in} .

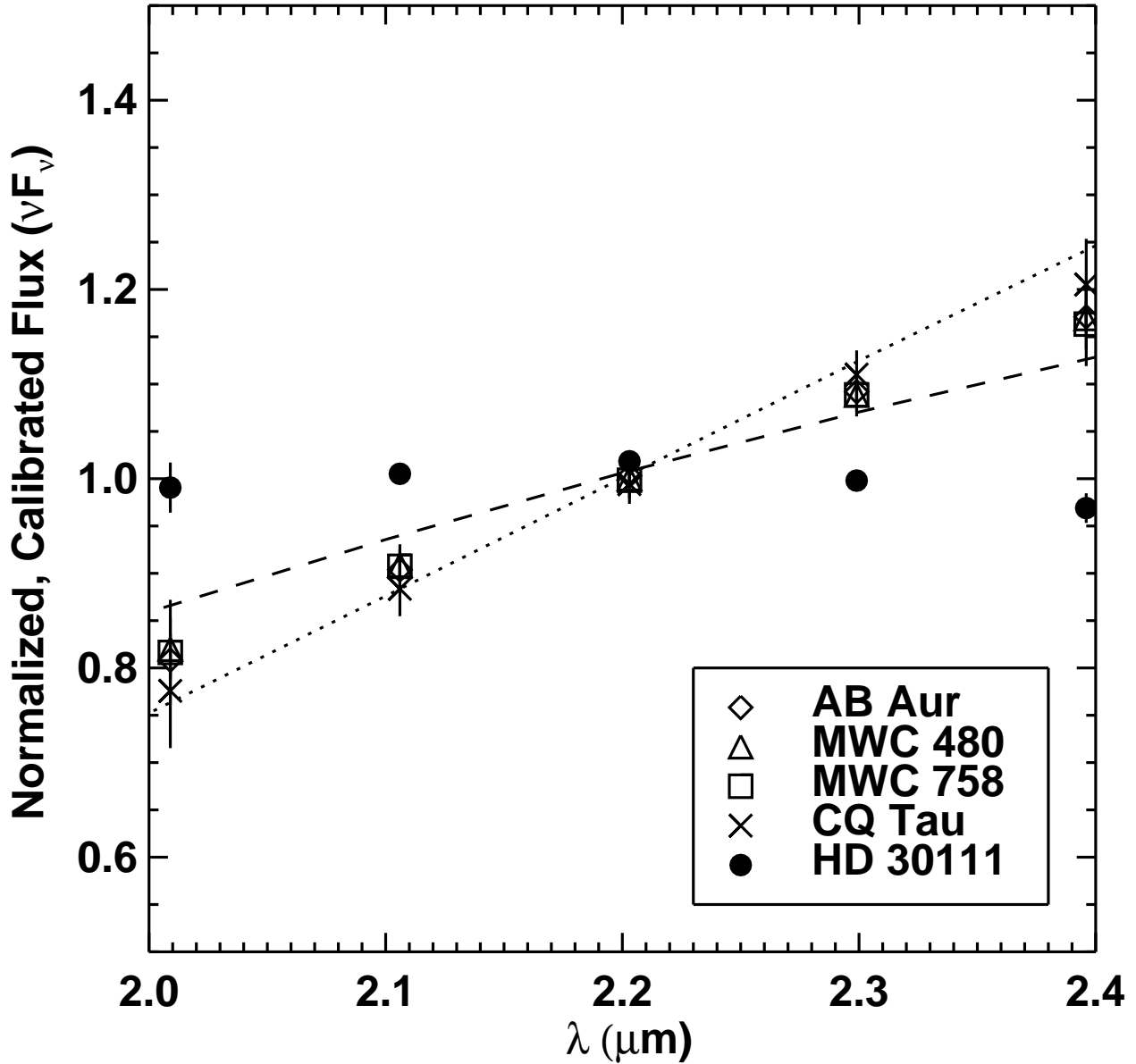


Fig. 1.— Normalized, calibrated photometry for four Herbig Ae/Be stars and one “check star,” HD 30111. We display these objects because the photometry for all sources was calibrated using the same set of three main-sequence calibrator stars, allowing examination of systematic calibration effects. The check star, which has a spectral type of G8III ($H - K \sim 0.1$ from 2MASS), exhibits a nearly flat spectrum across the K -band, illustrating that our calibration is reliable. The photometry for our target sources shows no evidence of narrow-band emission features, and the observed spectral slopes for these objects are comparable to those of blackbody disk models where the temperature of the hottest material is between 1200 K (dotted line) and 1600 K (dashed line).

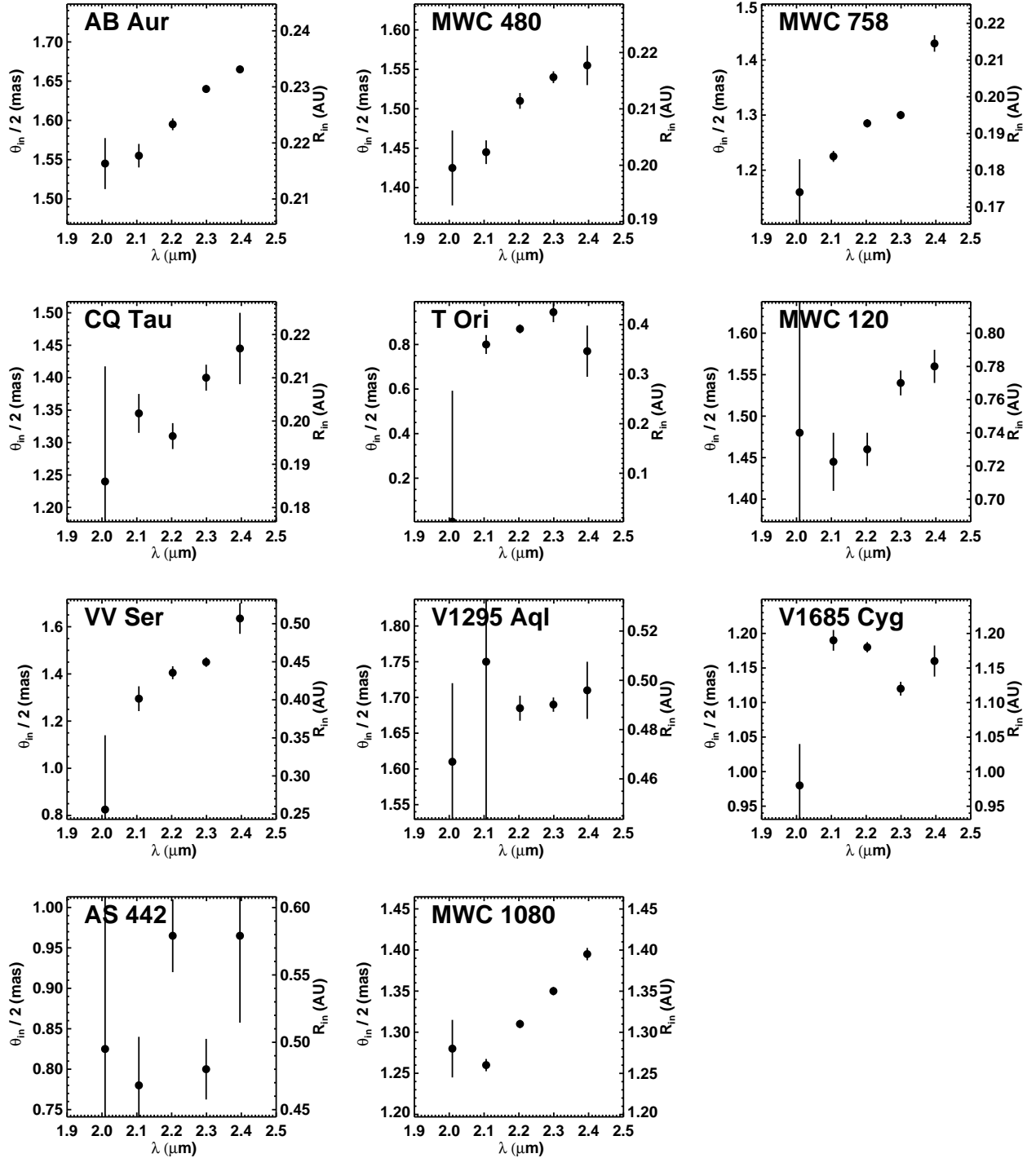


Fig. 2.— Inner ring radii, $\theta_{\text{in}}/2$, as a function of wavelength, as determined from inclined uniform ring models fitted to the data in individual spectral channels. We also provide the linear inner ring radii, R_{in} , computed using assumed distances for these objects (Eisner et al. 2004, and references therein). Inclinations, position angles, and ring widths were assumed (§3.2), and the inner ring radius was the only free parameter in the model fitting.

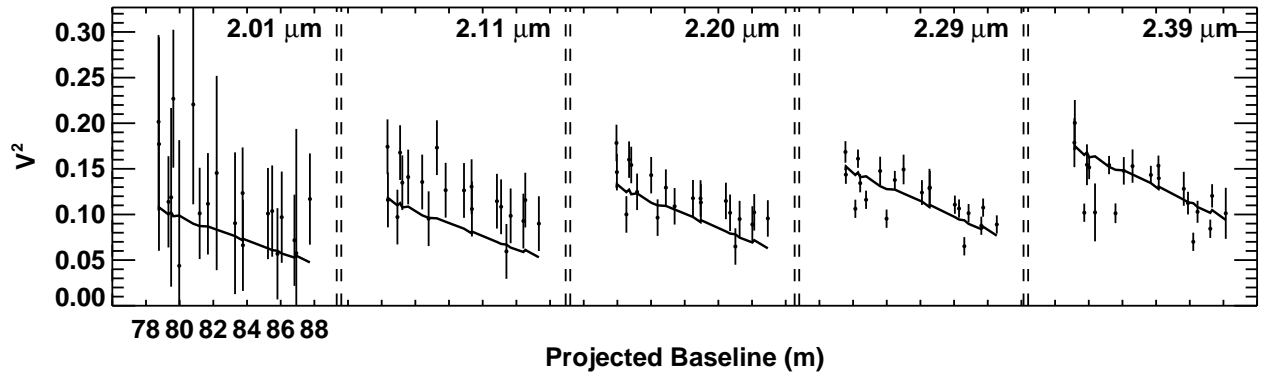


Fig. 3.— PTI V^2 data for AB Aur plotted with the best-fit single-temperature ring model (§3.3.1). The model systematically under-predicts the data in the short-wavelength channels. The reduced χ^2 of the fit for this object, and all other objects in our sample, is > 1 , indicating poor agreement between this simple model and the data.

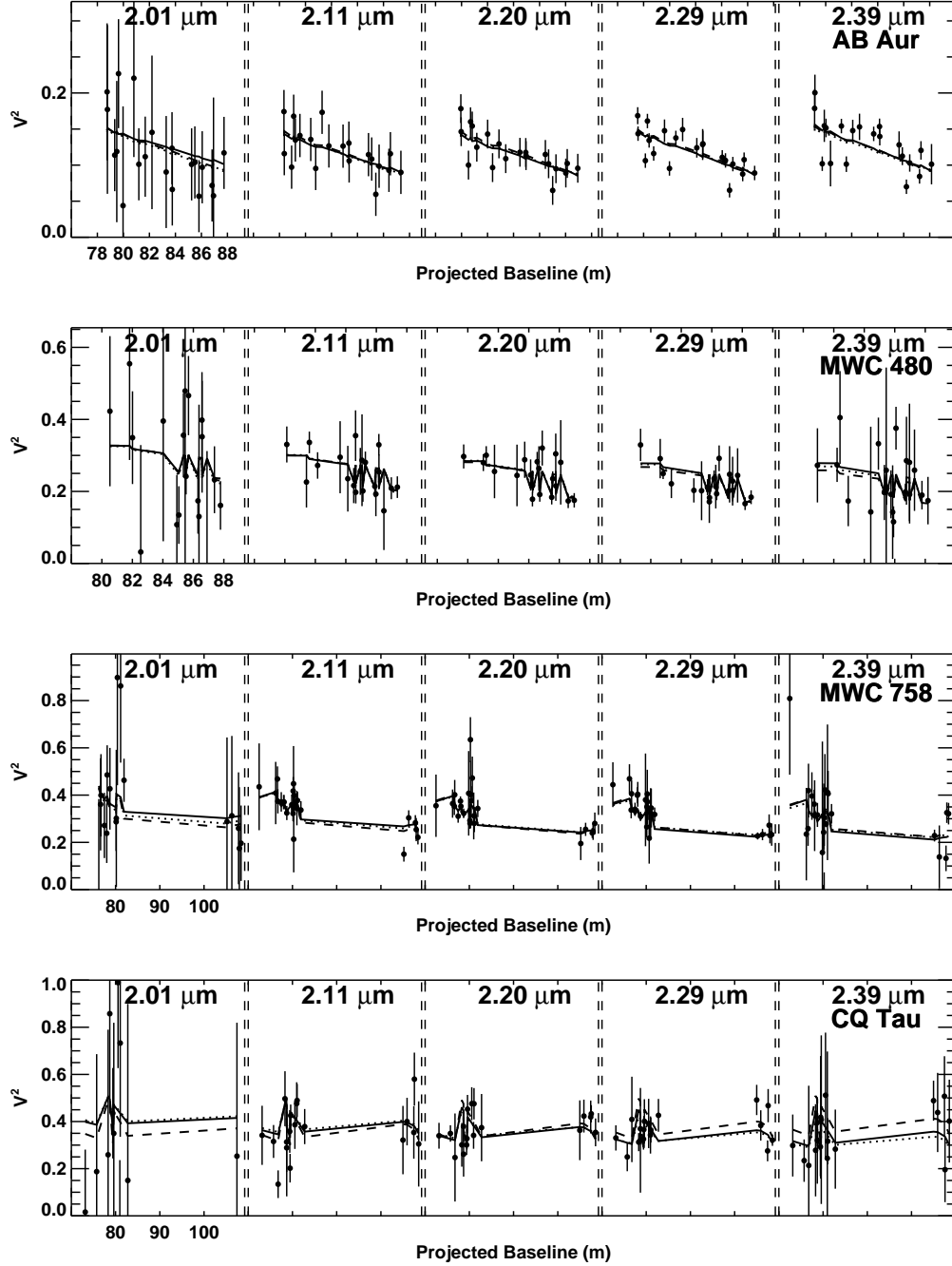


Fig. 4.— PTI V^2 data (points), and best-fit models. Two-ring models are represented by solid lines. Disk models incorporating smooth temperature gradients are indicated by dotted lines. Dashed lines show the best fits obtained when only the second and third channels (“continuum”-only fits) were used to constrain the fits of these disk temperature-gradient models. Data for multiple baselines, with multiple position angles on the sky (§2), are plotted here. Curves for best-fit models may therefore have a jagged appearance since inclined disks have different visibilities when observed at different position angles.

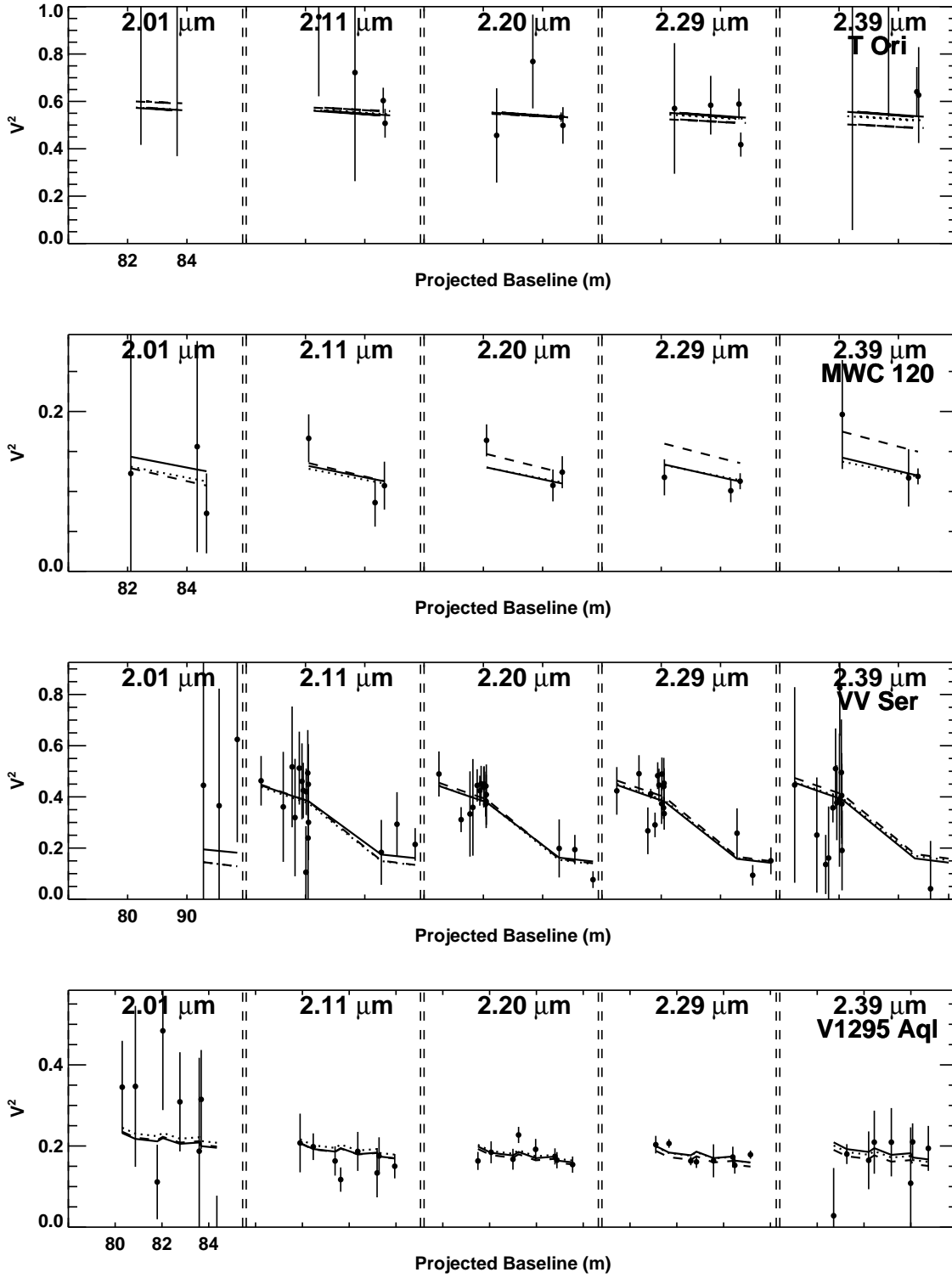


Fig. 4. — continued.

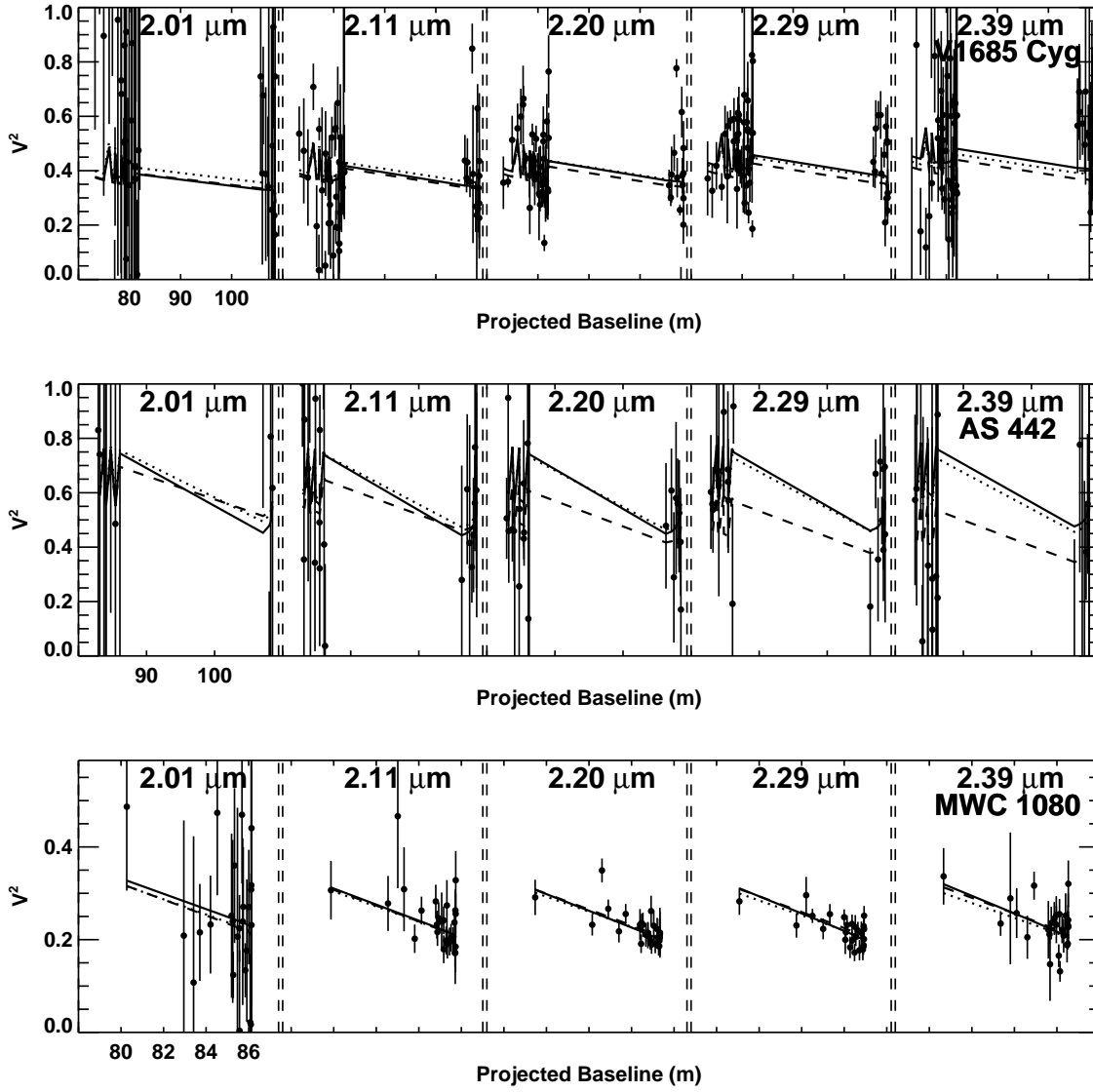


Fig. 4. — continued.

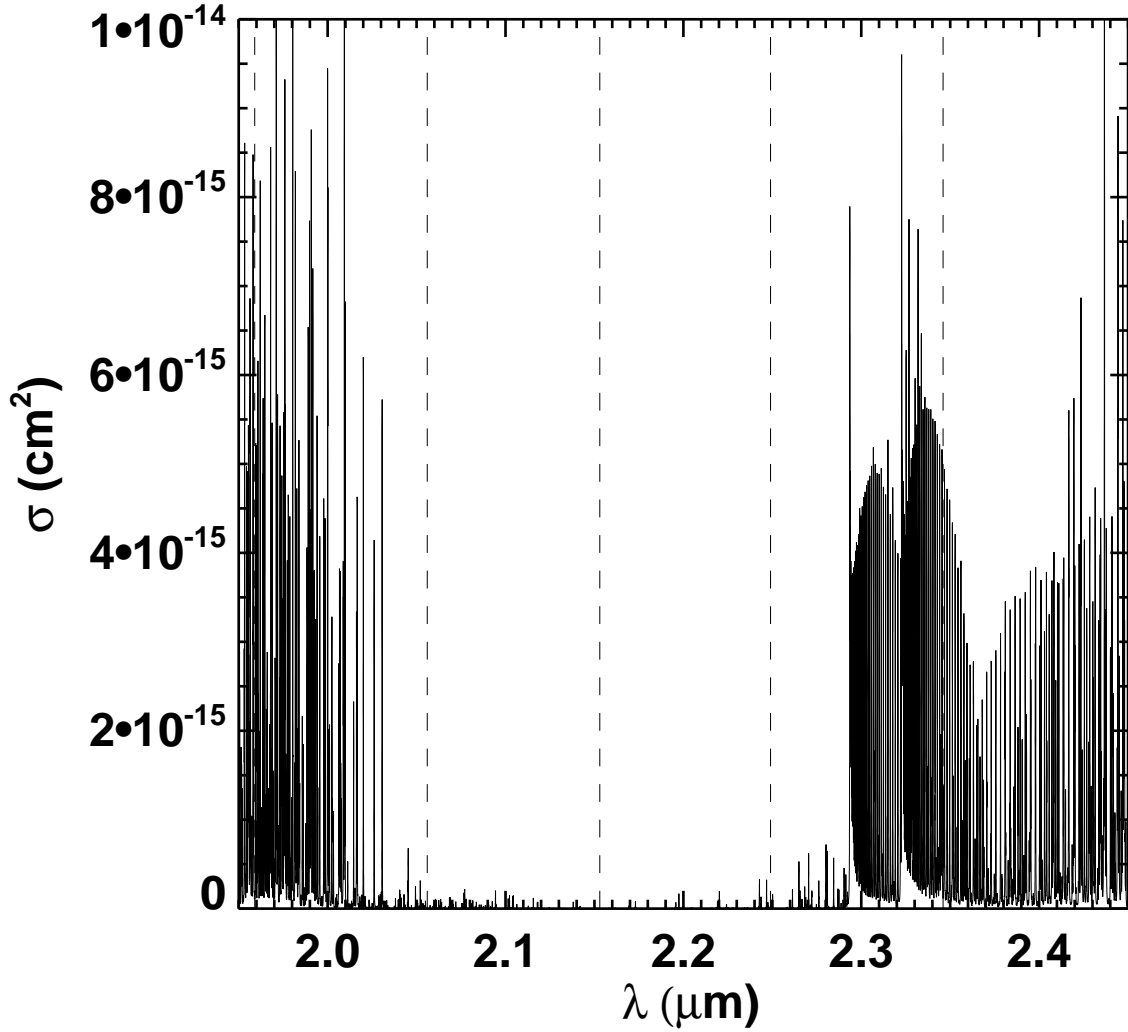


Fig. 5.— Radiative cross sections (σ) for water and CO in the *K*-band spectral region (solid line). Lines are drawn from the HITRAN database for temperature $T = 3000$ K (Rothman et al. 2005), and convolved with Voigt profiles assuming molecular number densities of $n = 10^{19} \text{ cm}^{-3}$. The boundaries of the spectral channels used in this paper are indicated with dashed lines.

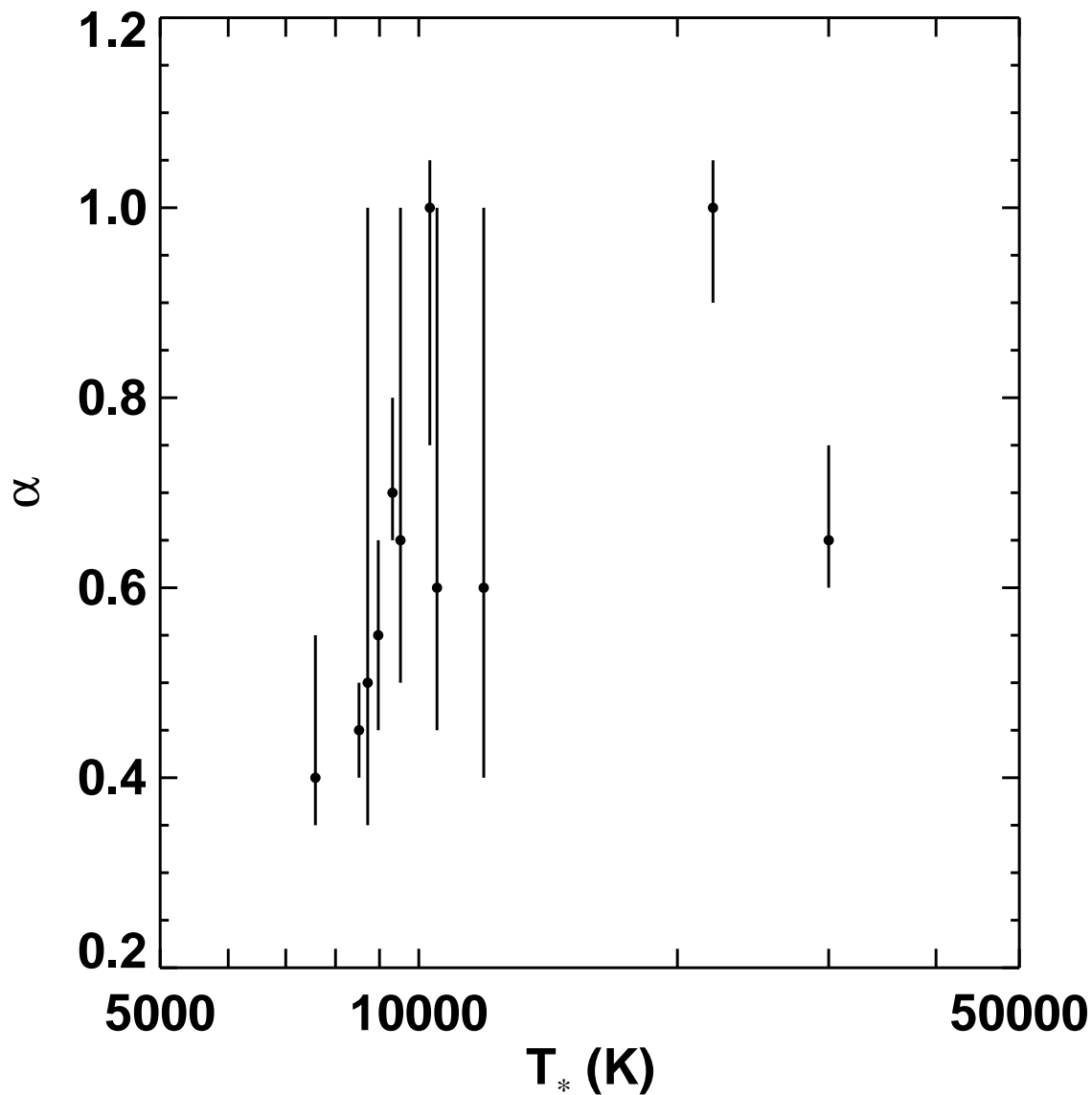


Fig. 6.— Best-fit values of α for disk models with a power-law temperature gradient, as a function of stellar effective temperature, T_* . Although the uncertainties on α are large for some objects, the data suggest that disks around cooler stars tend to have shallower temperature gradients than disks around hotter stars. T_* is based on the assigned spectral types from Eisner et al. (2004). For objects with the same T_* , we have introduced an arbitrary offset of 200 K for ease of viewing.

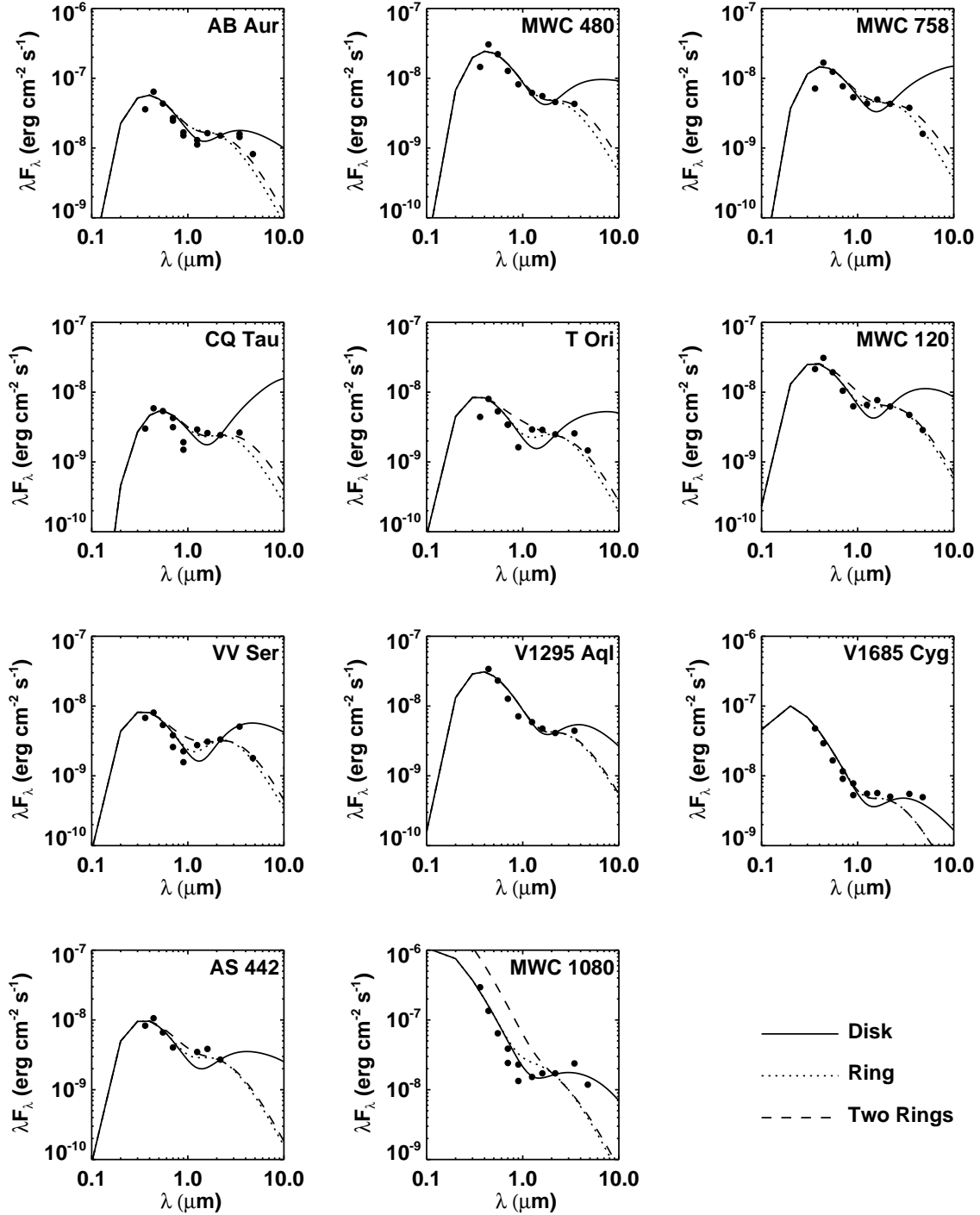


Fig. 7.— SEDs computed for our best-fit models. SED data from the literature (Eisner et al. 2004, and references therein) are indicated with filled circles, disk models with power-law temperature profiles are shown with solid lines, single-temperature ring models are represented by dotted lines, and two-ring models are shown as dashed lines.